Interactions of ENSO, the IOD, and the SAM in CMIP3 Models

WENJU CAI, ARNOLD SULLIVAN, AND TIM COWAN

CSIRO Marine and Atmospheric Research, Aspendale, Victoria, Australia

(Manuscript received 23 March 2010, in final form 19 October 2010)

ABSTRACT

Simulations of individual global climate drivers using models from the Coupled Model Intercomparison Project phase 3(CMIP3) have been examined; however, the relationship among them has not been assessed. This is carried out to address several important issues, including the likelihood of the southern annular mode (SAM) forcing Indian Ocean dipole (IOD) events and the possible impact of the IOD on El Niño–Southern Oscillation (ENSO) events. Several conclusions emerge from statistics based on multimodel outputs. First, ENSO signals project strongly onto the SAM, although ENSO-forced signals tend to peak before ENSO. This feature is similar to the situation associated with the IOD. The IOD-induced signal over southern Australia, through stationary equivalent Rossby barotropic wave trains, peak before the IOD itself. Second, there is no control by the SAM on the IOD, in contrast to what has been suggested previously. Indeed, no model produces a SAM–IOD relationship that supports a positive (negative) SAM driving a positive (negative) IOD event. This is the case even in models that do not simulate a statistically significant relationship between ENSO and the IOD. Third, the IOD does have an impact on ENSO. The relationship between ENSO and the IOD in the majority of models is far weaker than the observed. However, the ENSO's influence on the IOD is boosted by a spurious oceanic teleconnection, whereby ENSO discharge–recharge signals transmit to the Sumatra–Java coast, generating thermocline anomalies and changing IOD properties. Without the spurious oceanic teleconnection, the influence of the IOD on ENSO is comparable to the impact of ENSO on the IOD. Other model deficiencies are discussed.

1. Introduction

The global climate is influenced by several major climate drivers, including the El Niño–Southern Oscillation (ENSO) (Philander 1990), the southern annular mode (SAM, also called the Antarctic Oscillation) (Wallace and Thompson 2002), and the Indian Ocean dipole (IOD) (Saji et al. 1999; Webster et al. 1999). Using outputs from the Coupled Model Intercomparison Project phase 3 (CMIP3), recent studies have examined climate model simulations of the IOD (Saji et al. 2006; Cai et al. 2009a,b), ENSO (Joseph and Nigam 2006; Guilyardi 2006; Guilyardi et al. 2009), and the SAM (Raphael and Holland 2006; Cai and Cowan 2007); however, model performance in terms of their relationships in the multimodel space has not been assessed. As we will show, such an examination will help address several important issues, including whether the SAM drives the IOD, or whether the IOD influences ENSO.

Throughout the paper, a simple test is used: if mode A has an influence on mode B, then in models with a greater amplitude of A, the coherence (correlation) between A and B will be greater; therefore, the intermodel variations in the amplitude of mode A versus intermodel variations of their coherence is statistically significant. It is important to emphasize that this is only a **necessary** condition for the possibility that mode A has an impact on mode B. If the condition is met, then a physically plausible process must also be identified. If this condition is not met, then it is unlikely that mode A has an impact on mode B.

Several recent studies have investigated various impacts of ENSO on the Southern Hemisphere (SH). For instance, there are well-established linkages in terms of zonal wavenumber 3 and wavenumber 1 of the subpolar circulation (Kidson and Renwick 2002; Cai and Baines 2001; Hobbs and Raphael 2007) through the so-called Pacific–South America (PSA) pattern (Karoly 1989). L'Heureux and Thompson (2006) found a strong linear relationship between the SAM and ENSO, particularly in the austral summer months (November–February), and showed that the impact of ENSO is through both thermally forced and eddy-driven zonal wind anomalies. L'Heureux and

Corresponding author address: Wenju Cai, CSIRO Marine and Atmospheric Research, PMB 1, Aspendale VIC 3195, Australia.
E-mail: wenju.cai@csiro.au

DOI: 10.1175/2010JCLI3744.1

Thompson (2006) concluded that a significant portion of SH circulation variability on interannual time scales is ENSO driven.

Conversely, it has been suggested that tropical ENSO variability can be influenced by variations of circulation fields (e.g., sea levels) near the Drake Passage (Ivchenko et al. 2004, 2006) through an oceanic pathway, whereby a perturbation propagates in a wavelike manner in the form of fast-moving barotropic oceanic Rossby waves from the Drake Passage to the western Pacific in only a few days. This signal is then reflected at the western boundary of the South Pacific and generates a coastally trapped Kelvin wave moving equatorward, eventually reaching the equator. This, in conjunction with a significant correlation between sea level or transport variations at the Drake Passage and the SAM (Hughes et al. 2003; Meredith et al. 2004; Vivier et al. 2005), presents an unclear picture regarding the relationship between the SAM and ENSO. The notion that ENSO is a forcing of SH variability appears to be weakened by the fact that a PSA mode tends to peak before ENSO. Jin and Kirtman (2009) demonstrated that this is due to the seasonal cycle of the SH circulation and ENSO. If the phase of ENSO is shifted by 6 months to peak in June–August (JJA), as realized in their model, then the SH response becomes in phase with ENSO.

The relationship between the IOD and the SAM is just as unclear. A lag correlation between the IOD and mean sea level pressure (MSLP) anomalies south of Australia was invoked to suggest that the SAM is a driver of the IOD through IOD–conducive wind anomalies (Lau and Nath 2004). Because MSLP anomalies south of Australia peak before the mature phase of the IOD in September–November (SON), and are correlated with the SAM, the inference is that the SAM is a driver of the IOD. We use our simple test to examine this relationship.

In terms of an ENSO–IOD relationship, most studies have focused on the response of the Indian Ocean to ENSO through three different teleconnection processes. One process is an atmospheric teleconnection that modulates the thermodynamic fluxes at the sea surface (Klein et al. 1999; Yulaeva and Wallace 1994; Alexander et al. 2002), forcing basinwide sea surface temperature (SST) anomalies following an ENSO event, and easterly and heat flux anomalies conducive to the IOD during austral winter and spring. The second process involves off-equatorial Rossby waves excited by ENSO-induced wind stresses (Xie et al. 2002). The slow westward propagation of Rossby waves prolongs the ENSO influence on Indian Ocean SSTs seasons after the demise of ENSO. This leads to a capacitor-like effect in the Indian Ocean, as it slowly exerts a climatic impact in the surrounding regions in austral winter and spring (Xie et al. 2009). The third process involves the propagation of Pacific anomalies from the western Pacific into the Indian Ocean. This oceanic teleconnection is conducted through the Indonesian Throughflow passage, whereby ENSO signals transmit to the Indian Ocean arriving at the northwest Australia (NWA) coast and then radiate into the Indian Ocean interior. The transmission consists of two pathways: an equatorial Pacific wave pathway, in which equatorial Rossby waves become coastally trapped near where the western New Guinea coast intersects the equator in the west Pacific (Clarke and Liu 1994; Potemra 2001; Wijffels and Meyers 2004); and a subtropical North Pacific (NP) wave pathway (Cai et al. 2005; Shi et al. 2007), in which off-equatorial NP Rossby waves associated with ENSO impinge on the western boundary and move equatorward along the pathway of Kelvin–Munk waves (Godfrey 1975).

More recent studies suggest that significant interaction exists between the development of the IOD and ENSO; for example, a positive IOD may modify the amplitude/evolution ENSO by inducing wind anomalies associated with the Walker circulation (Saji and Yamagata 2003a,b; Li et al. 2003; Kug and Kang 2006; Behera et al. 2006) and vice versa. Such an interbasin coupling is crucial to both extreme positive IOD and El Niño predictions. In particular, accurate predictions of the IOD (El Niño) signal greatly enhance the El Niño (IOD) onset forecast (Luo et al. 2008, 2010). Are CMIP3 models as an entity able to simulate their mutual influence?

2. Data and models

We take one twentieth-century simulation of 50 yr (1950–99) from each of the available 24 CMIP3 models to provide a large intermodel space of a multicentury realization. The twentieth-century outputs of SST, MSLP, and thermocline (D20, depth of the 20°C isotherm) anomalies are linearly detrended and interpolated onto a common grid (0.8° × 1.9°). For each model, the outputs are stratified into four seasons with austral autumn as March–May (MAM), and so on.

Previous studies (Cai et al. 2009a,b) have identified five models [ECHAM and the global Hamburg Ocean Primitive Equation (ECHO-G), L'Institut Pierre-Simon Laplace Coupled Model, version 4 (IPSL CM4), Goddard Institute for Space Studies Atmosphere–Ocean Model (GISS-AOM), GISS Model E-R (GISS-ER), and Institute of Numerical Mathematics Coupled Model, version 3.0 (INM-CM3.0)] in which the IOD pattern is rather unrealistic. Thus, throughout our analysis these models are excluded. For each of the remaining 19 models, the three modes are identified by applying empirical orthogonal

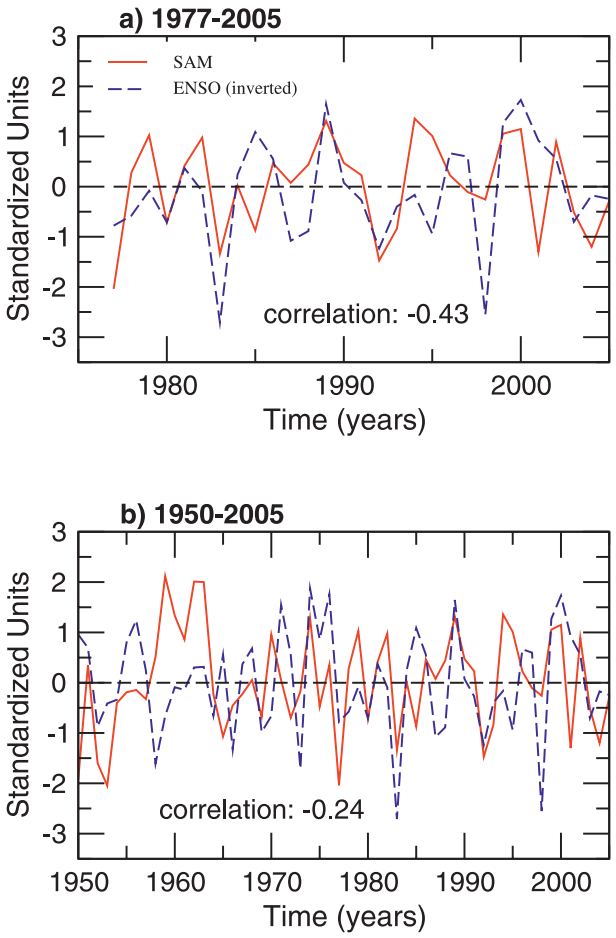

FIG. 1. Time series of the DJF SAM and ENSO indices over the periods (a) 1977–2005 and (b) 1950–2005, based on EOF analysis. The ENSO index is inverted for comparison to the SAM index.

function (EOF) analysis on detrended SST anomalies in the tropical Indian Ocean domain for the IOD (20°S–20°N, 40°–120°E) and in the tropical Pacific domain for ENSO (20°S–20°N, 120°E–80°W), and on MSLP anomalies for the SAM (40°–70°S). This is carried out for each season for each model, although the IOD only operates in JJA and SON. The associated time series are taken as the indices of these modes. EOF analysis is preferred to using standard indices such as Niño-3.4 and the dipole mode index (DMI), as it allows each model to show their patterns, as opposed to an imposed structure.

In our EOF analysis, the variance is expressed in the EOF pattern, and the amplitude is calculated as the standard deviation of the spatial variance, so that the associated time series has a standard deviation value of one. Throughout this study, a positive SAM index value refers to a phase when MSLP is anomalously high in the midlatitudes but low in the high latitudes, a positive IOD index value refers to a phase when SST anomalies are anomalously cold in the eastern Indian Ocean, and a positive ENSO index value refers to an El Niño phase.

An important feature of the model IOD is that the majority of the models generate an amplitude of cold anomalies in the Sumatra–Java upwelling region that is greater than the positive anomalies in the western IO, because of a Bjerknes-like positive feedback involving anomalous SSTs, winds, and the thermocline in the east (Saji et al. 1999; Webster et al. 1999). The majority of models produce an IOD variance stronger than that in the observed, meaning that the east–west SST gradient is stronger than the observed but with a reasonable IOD pattern.

For MSLP and geopotential height measurements, we use reanalyses from the National Centers for Environmental Prediction (NCEP) (Kalnay et al. 1996) to help benchmark the performance of models. A reconstructed SST reanalysis product [Met Office Hadley Centre Sea Ice and Sea Surface Temperature (HadISST)] (Rayner et al. 2003) is used to construct an index of the IOD [the DMI, defined by Saji et al. (1999)] and ENSO through EOF analysis as discussed above. Although these data are taken to represent observations, it is important to note that even within the 50-yr period that we focus on the relationship between the three modes varies vastly with time. For example, Fig. 1 displays the relationship between the SAM and ENSO indices in austral summer [December–February (DJF)] based on NCEP and HadISST, respectively. When based on data since 1977 (Fig. 1a), there is a statistically significant relationship (at the 95% confidence level), as in L'Heureux and Thompson (2006) using the November–February mean; an El Niño is associated with a negative SAM. But by extending the data back to 1950, the relationship weakens considerably (Fig. 1b). Using a station-based SAM index as in Marshall (2003), the relationship between SAM and ENSO is weaker in both periods.

3. The SAM and ENSO

Using the test outlined earlier, ENSO's influence on the SAM is produced in all seasons (Fig. 2). For each model, taking each of the 50 yr as independent samples, it would require a correlation coefficient of 0.27 between the SAM and ENSO to reach the 95% confidence level. Similarly, treating the 19 models as independent samples, a correlation coefficient of 0.43 is required to reach the 95% confidence level for the intermodel linear fit. Although strong intermodel variations exist, the intermodel linear fit is significant in most seasons and is strongest in austral spring (SON) and summer (DJF), when ENSO develops rapidly and matures. In most models, the correlation is such that when the ENSO index is positive, the SAM index is negative, yielding a negative correlation. In SON,

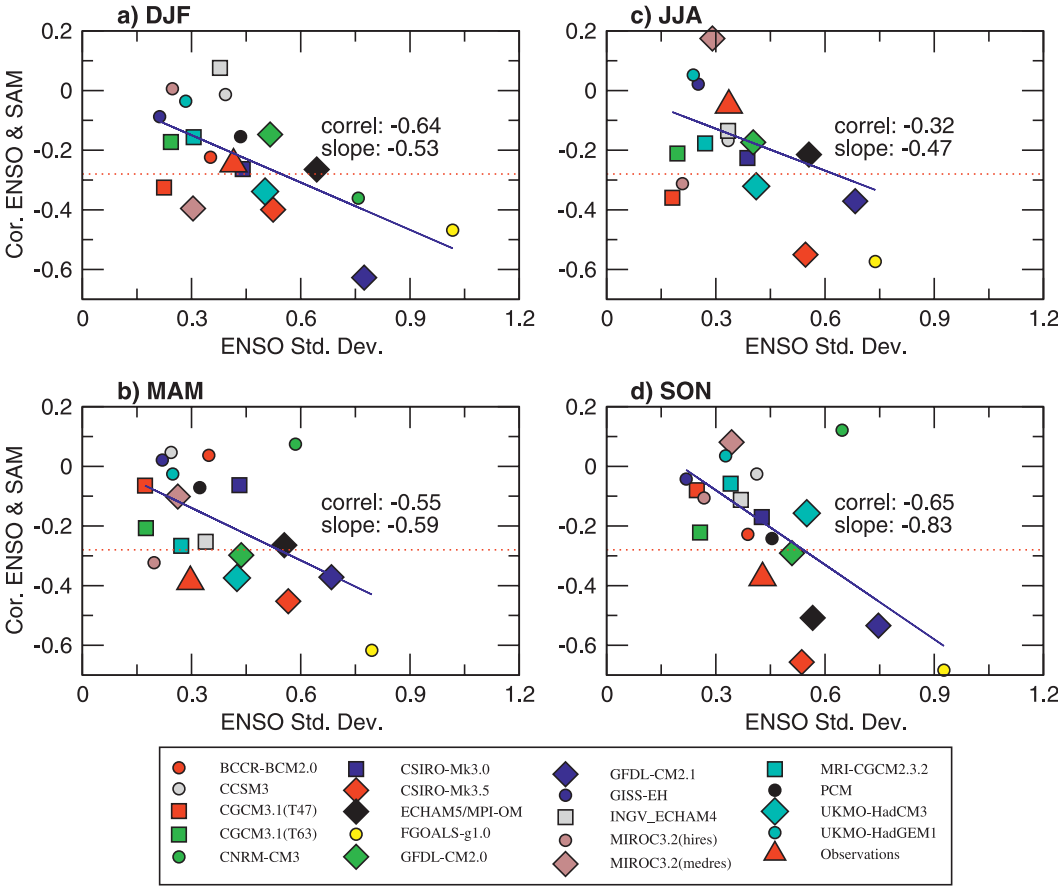

FIG. 2. Scatterplot of intermodel variations of ENSO–SAM correlations vs intermodel variations of ENSO amplitude for (a) DJF, (b) MAM, (c) JJA, and (d) SON. The ENSO–SAM correlations are calculated from the associated EOF time series, and the ENSO amplitude is the standard deviation of the EOF pattern. The dotted line represents the 95% confidence level for ENSO–SAM correlation coefficients.

only four models [Commonwealth Scientific and Industrial Research Organisation Mark version 3.5 (CSIRO Mk3.5), Geophysical Fluid Dynamics Laboratory Climate Model version 2.1 (GFDL CM2.1), Flexible Global Ocean–Atmosphere–Land System Model gridpoint version 1.0 (FGOALS-g1.0), ECHAM5/Max Planck Institute Ocean Model (MPI-OM)] produce a correlation that is greater than that based on NCEP reanalysis. A similar plot (Fig. 3), replacing ENSO amplitude with the amplitude of the SAM, shows that there is no control of the SAM on ENSO. Thus, our results support the idea that ENSO signals drive and project onto the SAM (L'Heureux and Thompson 2006).

The observed correlation in DJF (Fig. 1a) using NCEP is far smaller than that shown by previous studies. Using data for the period 1978–2003, L'Heureux and Thompson (2006) obtained a correlation of −0.52 for the average over November–February.

Because the control by ENSO on the SAM is present in most seasons, we apply EOF analysis to monthly MSLP to obtain a monthly SAM index (positive meaning high MSLP at the midlatitudes) and to SST to obtain an ENSO index (positive indicating El Niño) for the four models in which the ENSO–SAM correlation is generally greater than that from NCEP. Figure 4 shows that there is indeed a strong coherence, with all models exceeding the 95% confidence level based on the lag-1 month autocorrelation. An important feature is that while some of the SAM signals are forced by ENSO, the SAM peaks before ENSO in all but one of the four models. For example, the SAM leads ENSO by 2 months in the observations (Fig. 4e), by 3 months for ECHAM5–MPI-OM (Fig. 4d), and 1 month for GFDL CM2.1 (Fig. 4b). For FGOALS-g1.0 (Fig. 4c), ENSO peaks 1 month before the SAM with a correlation of 0.60 (although the concurrent correlation coefficient is comparable at 0.59) and may be linked to the fact that the ENSO amplitude is about 3 times as large as the observed. For CSIRO Mk3.5 (Fig. 4a), ENSO peaks concurrently with the SAM; as will be discussed below, in CSIRO Mk3.5, ENSO peaks

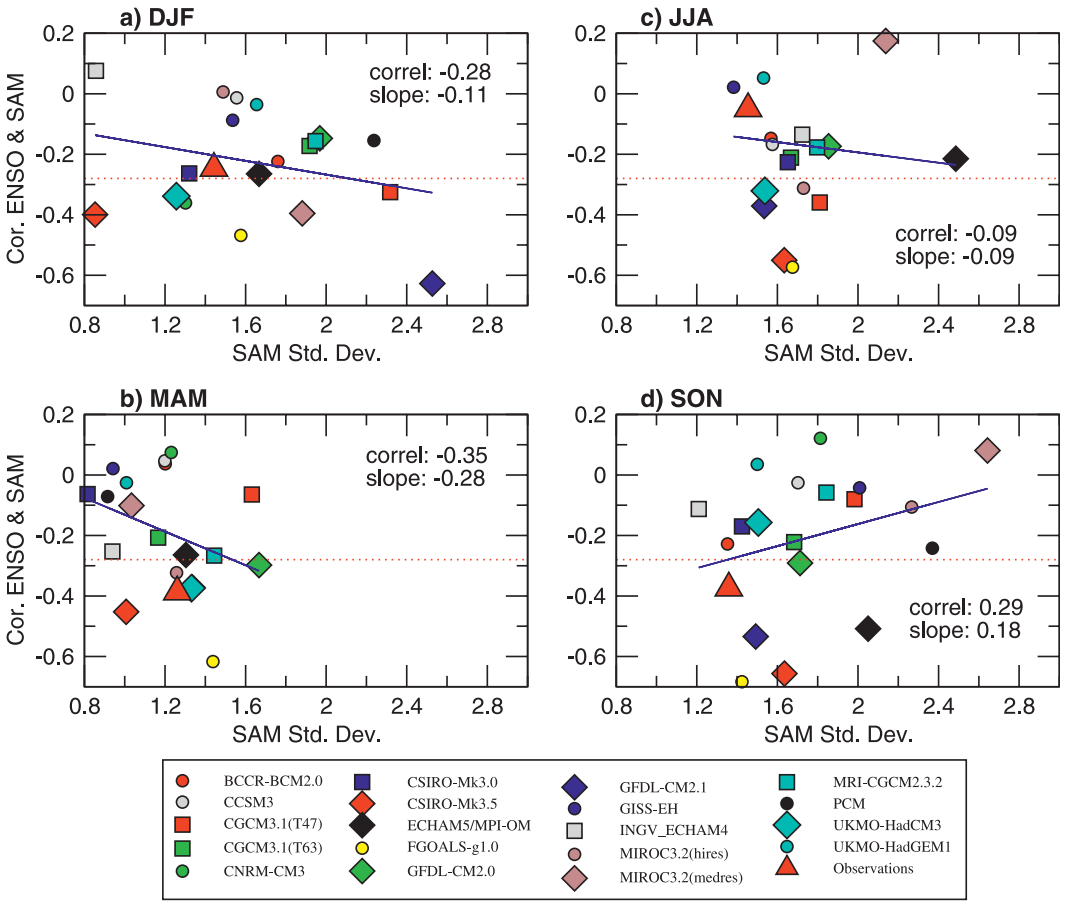

FIG. 3. As in Fig. 2, but for the SAM amplitude.

in May, rather than the observed DJF. This lead–lag relation is generally true for other modes, such as the two PSA patterns, as shown in Jin and Kirtman (2009) using NCEP data. Thus, although ENSO forces the SAM, the SAM tends to peak before ENSO.

To illustrate the ENSO–SAM lag relationship, we take ECHAM5–MPI-OM, in which ENSO peaks in DJF as in the observations, and conduct a lag correlation between the monthly SAM index and gridpoint MSLP and SST anomalies, at 3-month intervals. Three months before an El Niño peaks, the SAM is the dominant pattern (Figs. 5b and 5e) with large MSLP and SST anomalies highly zonally symmetric in the middle to high latitudes. Three months after the SAM peaks, ENSO reaches its mature phase with a Southern Oscillation pattern well defined (Fig. 5c) and strong cold SST anomalies in the equatorial Pacific (Fig. 5f). As discussed above, the lag is due to the seasonal cycle of a response in the SH circulation, which generally peaks in austral winter and spring, as opposed to the matured phase of ENSO in austral summer as illustrated by Jin and Kirtman (2009) for an ENSO-induced PSA pattern. This is confirmed by CSIRO Mk3.5, in which ENSO peaks in May, and no such lag is generated between the timing of the matured SAM and ENSO.

In summary, using our test, ENSO has an influence on the SAM, even though the SAM tends to peak earlier than ENSO. The SAM has little influence on the ENSO.

4. The SAM and the IOD

The majority of models produce a SAM variance stronger than in the observations. Likewise the IOD (which operates in JJA and SON) is stronger in the majority of the models (Fig. 6), meaning that the east–west SST gradient is stronger than the observed. Figures 6a and 6b examine a possible control by the SAM over the IOD in JJA and SON, respectively. The intermodel relationship between the SAM amplitude and the SAM–IOD correlation is small and not statistically significant in both seasons, implying that there is no forcing effect of the SAM on the IOD. This is in sharp contrast to the result suggesting that a positive SAM phase is conducive to a positive IOD (Lau and Nath 2004). In their study Lau and Nath (2004) showed that a circulation anomaly pattern associated with MSLP anomalies

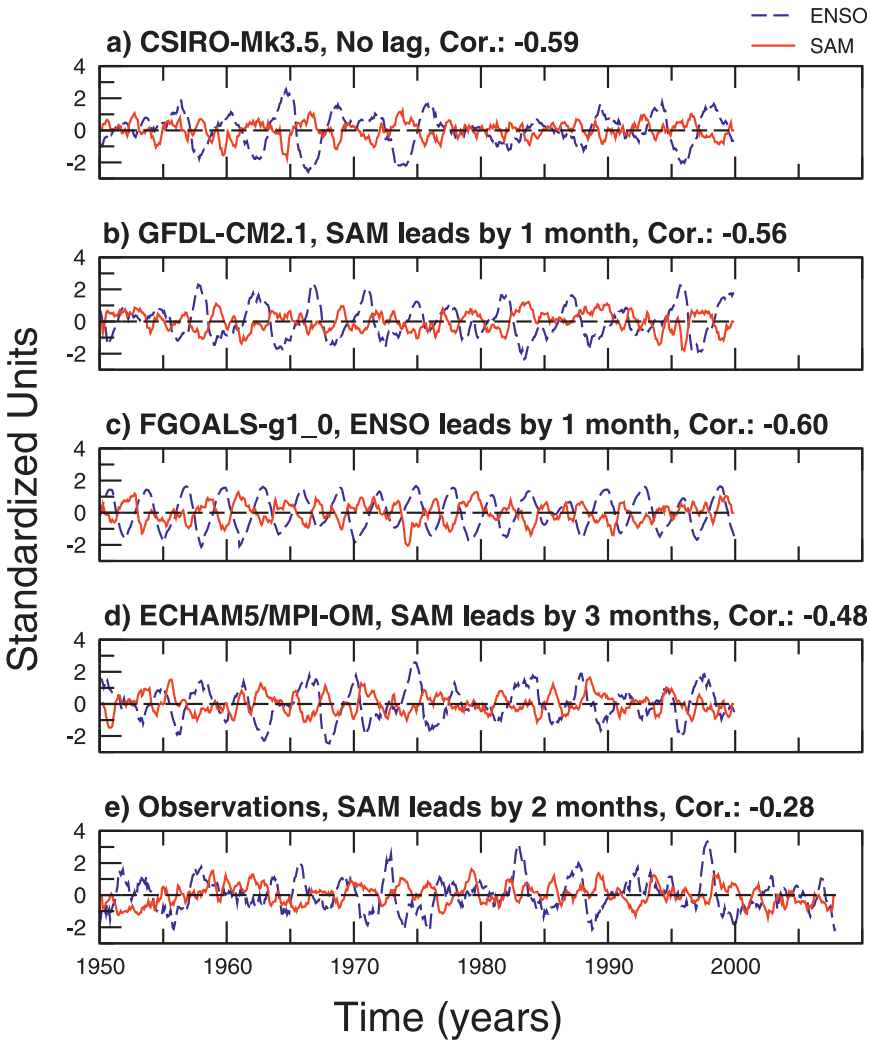

FIG. 4. Time series of ENSO and SAM indices for (a)–(d) 4 models and (e) observations, represented by the corresponding EOF monthly time series. Both time series are smoothed by 7 months.

averaged over 35°–50°S, 110°–165°E (which they termed the AUS index) is similar to that associated with the SAM. Southeasterly wind anomalies associated with the AUS index over the Sumatra–Java region promote upwelling and a shoaling thermocline, leading to a cooling in the eastern pole and eventually to a positive IOD.

Using HadISST and a SAM index, derived from EOF analysis on NCEP MSLP anomalies, we are able to reproduce the result of Lau and Nath (2004) associated the AUS index. For example, a simultaneous correlation of the AUS index with the SAM is 0.48 in JJA and 0.55 in SON, and their regression patterns of SLP and SST onto the AUS index [Lau and Nath (2004), their Figs. 9e and 9f] are similar to our correlation patterns (Figs. 7a and 7b). However, the MSLP pattern associated with the AUS index is confined to south of Australia (Fig. 7a).

One argument supporting the forcing of the IOD by anomalies represented by the AUS index (and hence by the SAM) is that the JJA AUS index leads the IOD index by one season. This IOD–AUS index lead–lag relationship means that the AUS index peaks before the IOD matures. This is indeed the case, and there is a better-defined IOD pattern with stronger western pole anomalies in SON (Fig. 7c) than in JJA (Fig. 7b). However, there is no statistically significant relationship between the SAM and the IOD in JJA (Fig. 7, right column). Correlation patterns associated with the SAM (Figs. 7e and 7f) are quite different from those associated the AUS index (Figs. 7b and 7c). There is little significant correlation with the SAM over the Indian Ocean. For that matter, the polarities in the Indian Ocean are generally opposite.

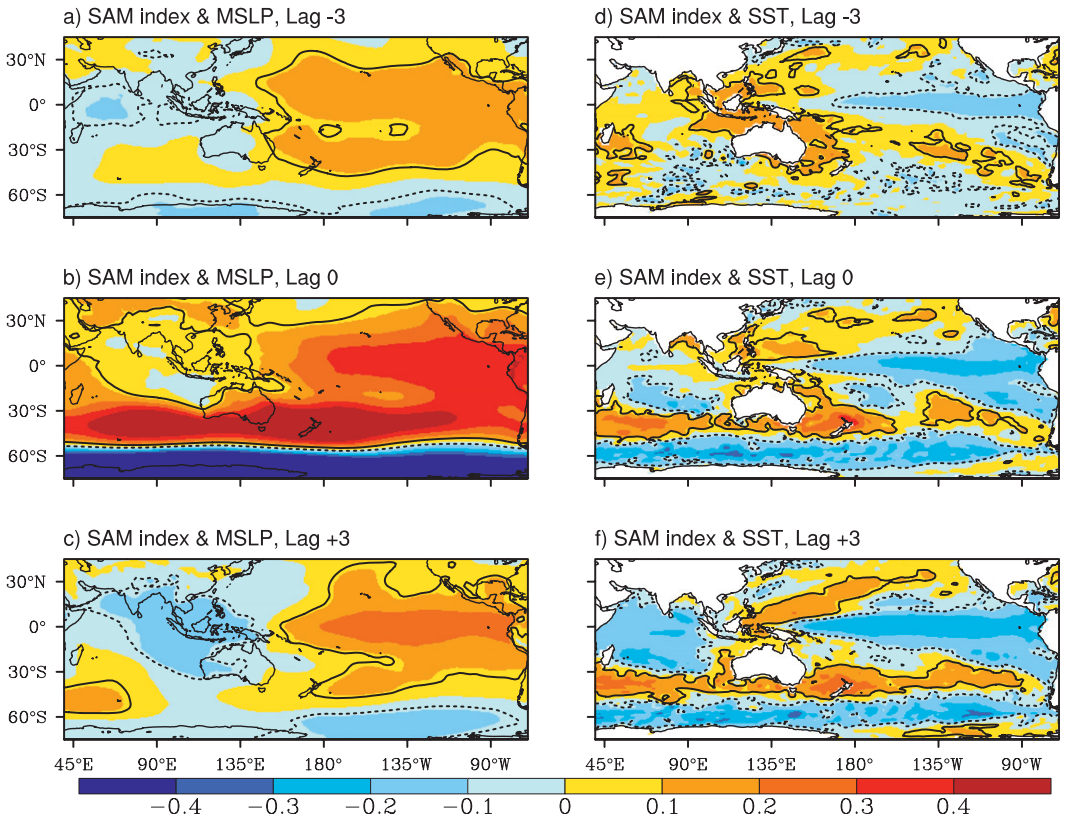

FIG. 5. Monthly lag correlation between the monthly SAM index (fixed) at 3-month intervals (lag −3 to +3) with (a)–(c) gridpoint MSLP and (d)–(f) SST as simulated in ECHAM5–MPI-OM. Areas confined by contours are statistically significant at the 95% confidence level.

In the multimodel space, there is no relationship between intermodel variations of JJA-SAM amplitude and JJA-SAM–SON-IOD correlations (Fig. 8). This is to test if the SAM leads the IOD in any of the models. No model produces a positive correlation that is statistically significant, whereas most produce a small negative correlation that is not statistically significant. Only 6 models [FGOALS-g1.0, CSIRO Mk3.5, GFDL CM2.0, GFDL CM2.1, National Center for Atmospheric Research Parallel Climate Model Version 1 (NCAR PCM1), and Met Office Hadley Centre Global Environmental Model version 1 (UKMO HadGEM1)] yield a statistically significant relationship, but in the sense that a negative SAM is linked to a positive IOD, in contrast to the relationship suggested by Lau and Nath (2004). In four of these models (FGOALS-g1.0, CSIRO Mk3.5, GFDL CM2.0, and, GFDL CM2.1), the ENSO–IOD (see Fig. 10, to be discussed in section 5) and ENSO–SAM (Fig. 2d) correlation are very high, supporting a common influence from ENSO. Lau and Nath (2004) noticed that in their model, the forcing by winds associated with the AUS index only operates when ENSO is weak or at a neutral phase. There are many models in which ENSO and the IOD are virtually not correlated, yet there is still no positive correlation between the SAM and the IOD {e.g., Canadian Centre for Climate Modelling and Analysis Coupled General Circulation Model, version 3.1 [CGCM3.1(T47)]}.

What then is the explanation of the AUS index–IOD relationship in the observations? Our hypothesis is that the anomalies associated with the AUS index are in fact generated by the IOD; like other anomalies induced by the tropics, they peak before the forcing itself (Jin and Kirtman 2009). Figure 9 shows the evolution of the one-standard-deviation anomaly pattern associated with the IOD using 3-month rolling mean anomalies, from JJA, JAS, ASO, and to SON. These are obtained by regressing detrended gridpoint anomalies onto the rolling IOD index and then multiplying the regression coefficients with the standard deviation value of the IOD index. The evolution of SST anomalies shows a strengthening of the positive phase of the IOD, as well as strong El Niño signals in the eastern Pacific (Figs. 9i–l).

In the positive IOD phase, cold SST anomalies suppress rainfall off the Sumatra–Java coast and drive an anticyclonic circulation anomaly that is consistent with

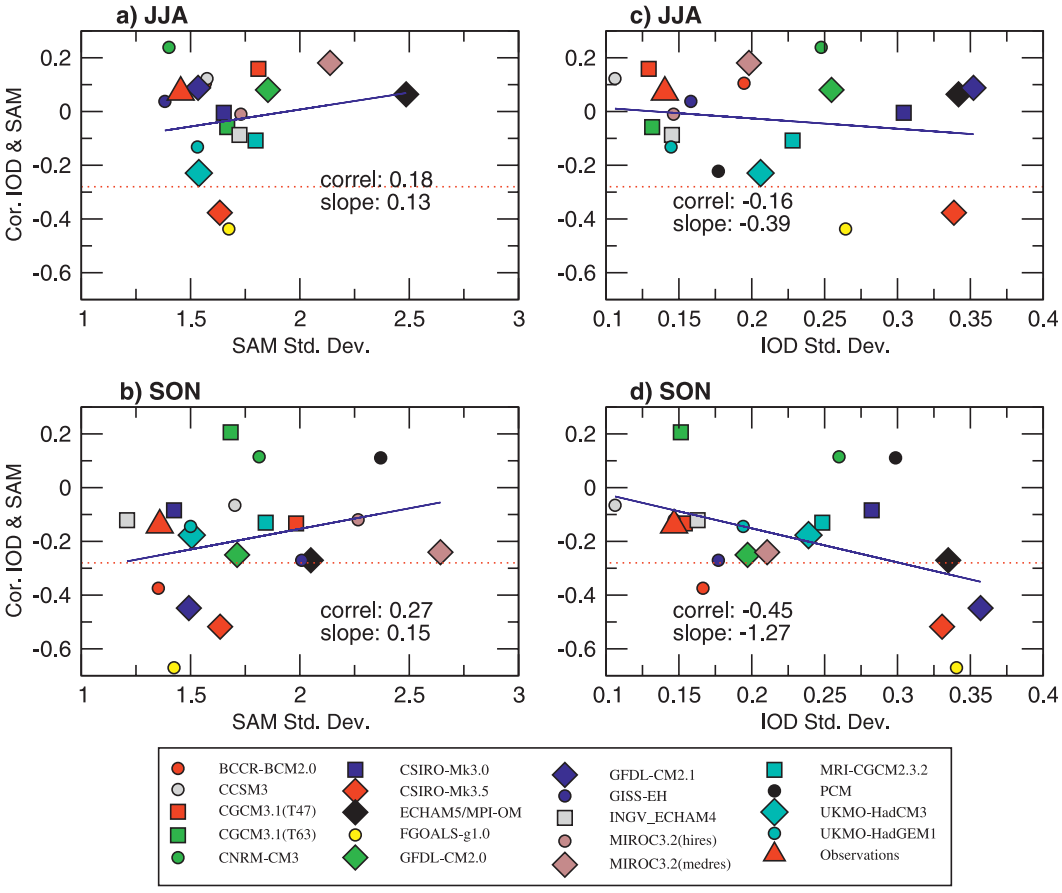

FIG. 6. Scatterplot of intermodel variations of SAM–IOD correlations vs intermodel variations of (a),(b) the SAM amplitude and (c),(d) the IOD amplitude for JJA and SON, respectively. The SAM–IOD correlations are calculated from the associated EOF time series, while their amplitudes are defined as the standard deviation of the associated EOF pattern. The dotted line represents the 95% confidence level for IOD–SAM correlation coefficients.

the steady response to a heat sink displaced south of the equator. The suppressed convection generates anomalous vertical motions, and the associated anomalous divergence acts as a Rossby wave source. In the tropics, the response is baroclinic (Gill model) but equivalent barotropic in the form of stationary Rossby wave trains in the extratropics (Hoskins and Karoly 1981).

The equivalent barotropic feature is evident through the MSLP anomaly patterns (Figs. 9a–d) that resemble those of height anomalies (Figs. 9e–h). These wave trains have a high pressure center south of Australia contributing to a high AUS index, with a tendency to contribute to a high-zonal-mean MSLP, therefore a higher SAM. They curve poleward west of the Drake Passage. That the generation is forced from the tropics is unambiguous. One important feature is that statistically significant anomalies appear first south of Australia during JJA, when the IOD starts to develop (Fig. 9a); anomalies downstream subsequently strengthen and become statistically significant as the IOD develops into its mature phase in SON (Figs. 9b–d), as indicated by Figs. 9i–l.

Returning to the multimodel variations, we notice that in the IOD prevalent season (SON), there appears to be a control by the IOD on the SAM (Fig. 6d). The control is largely a result of four models that contain a strong SAM–ENSO (section 3) and IOD–ENSO coherence (see section 5). The large IOD–SAM correlation arises from the fact that both are influenced by ENSO. When the ENSO influence is removed, the correlation weakens considerably (figure not shown).

Using outputs of the twentieth-century CMIP3 model experiments, Cai et al. (2009b) show that the pattern of the mean circulation change resembles that of a positive IOD, and that the mean change is accompanied by an increase in the positive IOD frequency (Cai et al. 2009a). Our result showing that the SAM is not a driver means that an upward trend of the SAM, as simulated by the majority of models, does not contribute to the IOD changes.

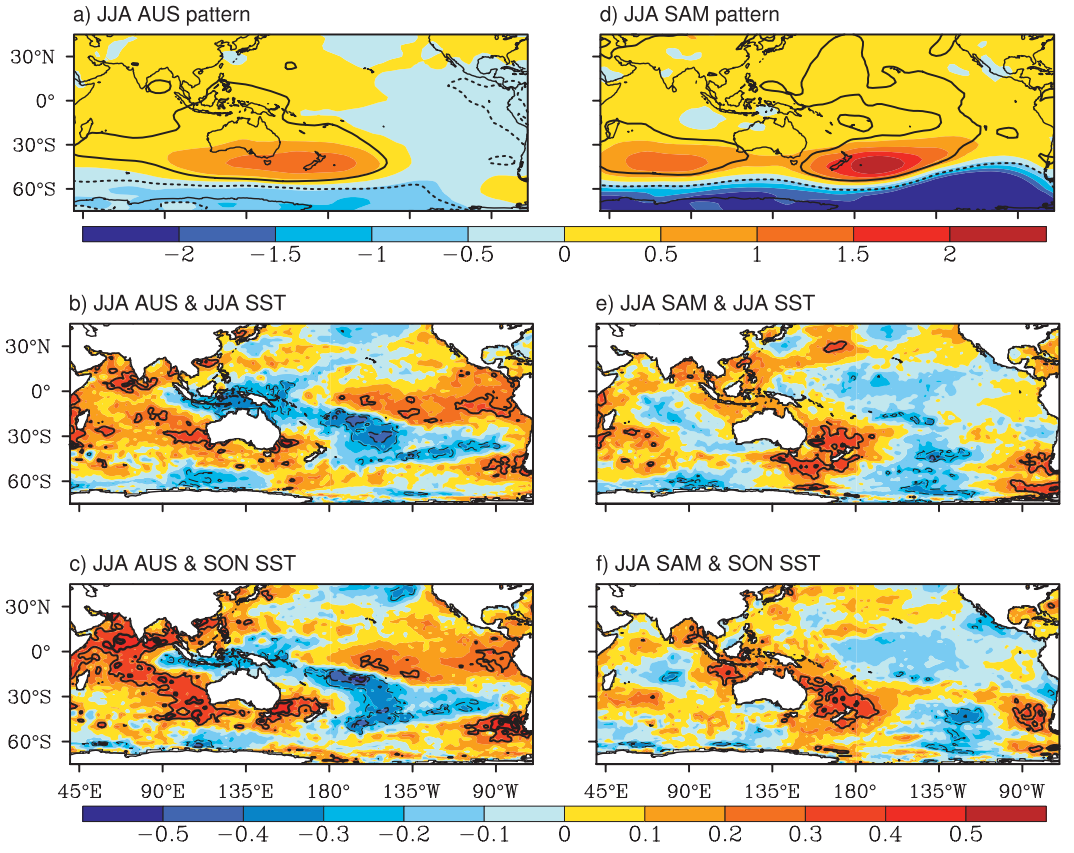

FIG. 7. MSLP pattern associated with (a) the JJA AUS index (regression coefficients in units of mb per mb); patterns of correlation between (b) JJA AUS index and JJA gridpoint SST and between (c) JJA AUS index and SON gridpoint SST. (d)–(f) As in (a)–(c), but for the SAM index. Areas confined by contours indicate statistical significance at the 95% confidence level.

5. ENSO and the IOD

Using CMIP3 models, previous studies (Saji et al. 2006; Cai et al. 2009c) showed that ENSO has a weak control over the IOD, supporting the notion that ENSO is not the sole forcing of the IOD and that other processes are involved. It turns out that in five models {Centre National de Recherches Météorologiques Coupled Global Climate Model, version 3 (CNRM-CM3), CSIRO Mk3.0, CSIRO Mk3.5, Bjerknes Center for Climate Research Climate Model version 2.0 (BCCR CM2.0), and Model for Interdisciplinary Research on Climate 3.2, medium-resolution version [MIROC3.2(medres)]}, the correlation between the IOD and ENSO is highest when ENSO leads by 1 yr. When this is taken into account, there is a strong control of ENSO over the IOD, particularly in SON, with a correlation of the linear fit at 0.62 (Fig. 10b), although most models produce an ENSO–IOD correlation that is too weak. The fact that this 1-yr lag is generated by several models suggests a common model deficiency (i.e., a spurious process). Replacing correlation at lag 0 for these five models, the correlation of the linear fit between the IOD and ENSO in SON is 0.48.

Before we focus on the common model deficiency, we note that the IOD's influence on ENSO is not much weaker

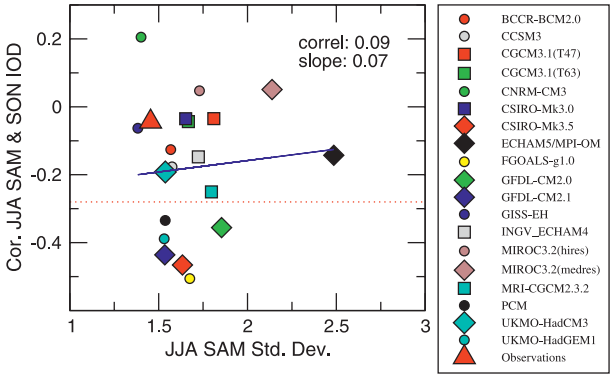

FIG. 8. Scatterplot of intermodel variations of SAM–IOD correlation vs intermodel variations of the SAM amplitude. The SAM is taken over JJA and the IOD over SON.

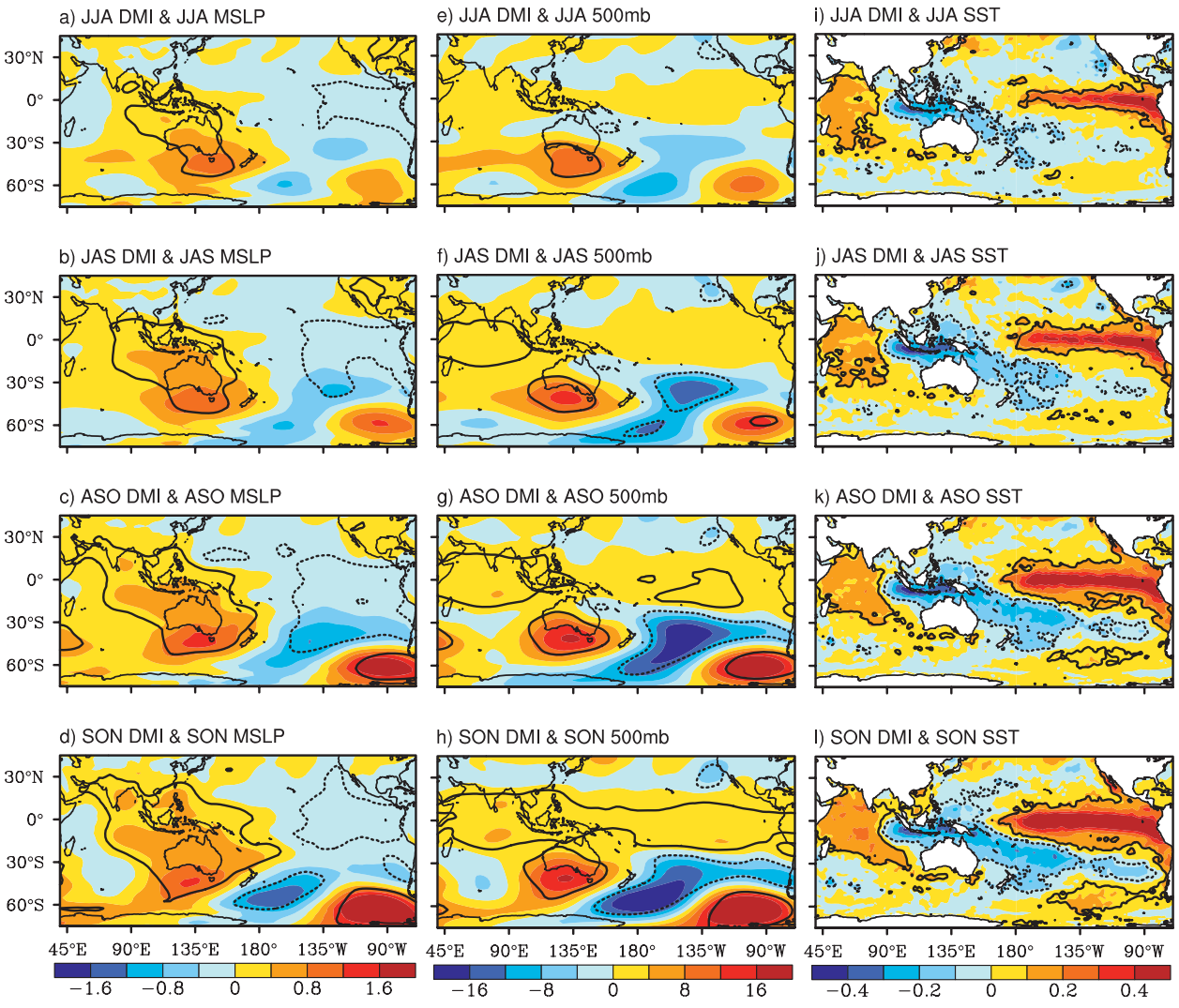

FIG. 9. Anomaly pattern obtained by regressing gridpoint anomalies onto an IOD index (DMI) for (left column) MSLP, (middle column) 500-mb geopotential height, and (right column) SST from June through November using 3-month rolling mean data. Areas confined by contours indicate statistical significance at the 95% confidence level.

than that of ENSO on the IOD (comparing Figs. 10a and 10b with Figs. 10c and 10d). In fact, in JJA, when the IOD develops, its influence on ENSO is actually stronger than ENSO's influence on the IOD (comparing Fig. 10a and 10c). Thus, CMIP3 models support the notion that the IOD can influence ENSO. Several recent studies suggest the IOD influence is achieved through a modification of the Walker circulation branches over the western Pacific and the nearby circulation (Li et al. 2003; Annamalai et al. 2005; Kug and Kang 2006; Luo et al. 2008), prolonging the lead time for ENSO prediction for up to 14 months before they peak (Izumo et al. 2010).

As discussed in the introduction, a process whereby an El Niño affects the IOD is through El Niño–induced easterly wind anomalies over the equatorial and eastern Indian Ocean. During May–October, these wind anomalies lead to a shallowing of the thermocline off Sumatra–Java, either by generating local upwelling or equatorial upwelling that propagates into the region. This then triggers a fast growth of the IOD through a Bjerknes-like positive feedback involving wind, SST, thermocline, and rainfall (Saji et al. 1999). Additionally, the easterly anomalies superimpose onto the climatological easterly flow to generate heat flux anomalies conducive for a rapid growth of the cooling anomaly in the eastern Indian Ocean (Hendon 2003).

ENSO signals also propagate into the Indian Ocean through oceanic teleconnections, whereby El Niño recharge–discharge signals propagate into the Indian Ocean, arriving at the NWA coast and then radiating

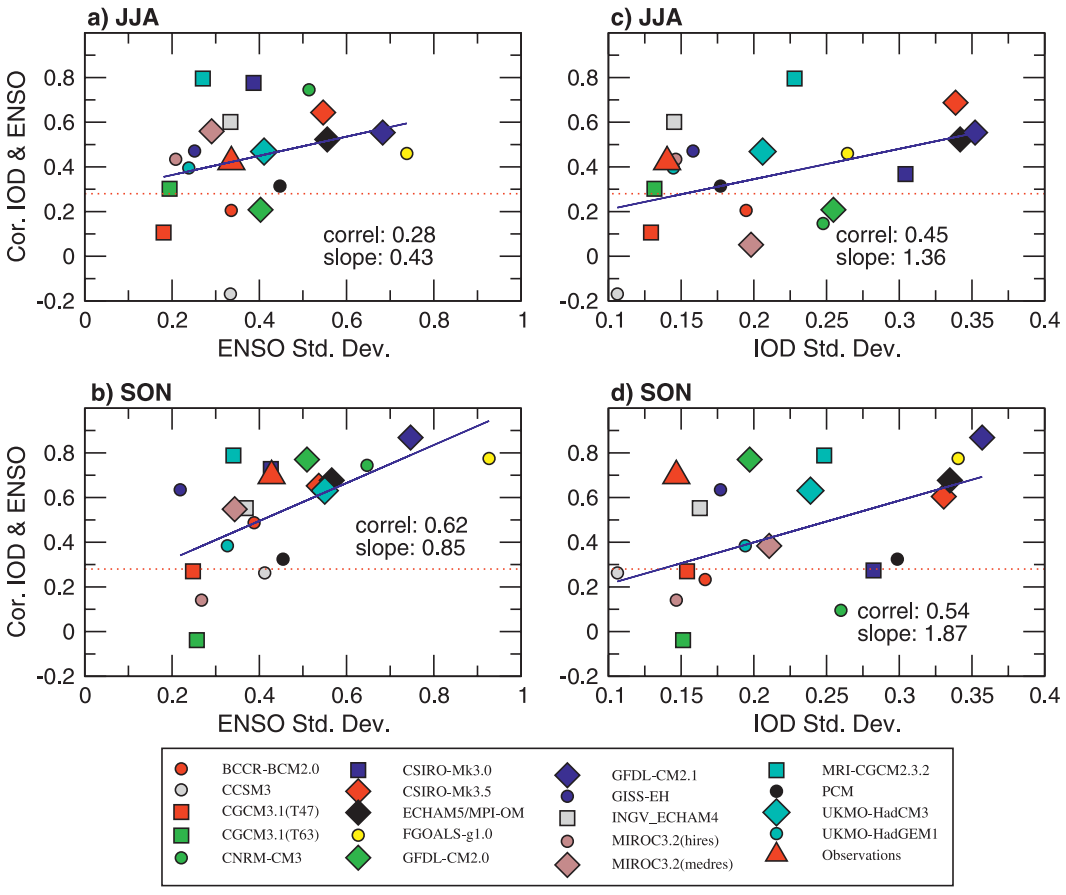

FIG. 10. Scatterplot of intermodel variations of ENSO–IOD correlations and ENSO amplitude for (a) JJA and (b) SON. (c),(d) As in (a),(b), but for the IOD amplitude. The ENSO–IOD correlations for (a) and (b) are taken as the maximum lag correlation but for (c) and (d) from a concurrent correlation. The ENSO and IOD amplitude is the standard deviation of the EOF pattern. The dotted line represents the 95% confidence level for IOD–ENSO correlation coefficients. Correlations between time series of IOD and ENSO peak at lag +1 year in CNRM-CM3, CSIRO Mk3.0, CSIRO Mk3.5, BCCR CM2.0, and MIROC3.2(medres).

into the interior (Wijffels and Meyers 2004; Cai et al. 2005; Shi et al. 2007). On a decadal or longer time scales, this teleconnection process can change the background state of the thermocline in the equatorial and eastern Indian Ocean (Shi et al. 2008), hence the properties of the IOD; however, there is little evidence of concurrent impact on the IOD by anomalies off the NWA coast.

Cai et al. (2005) found that in the CSIRO Mk3.0, the commencement of ENSO is late, such that during SON, the ENSO-induced wind anomalies are weak; in addition, there is a low sensitivity of the latent heat flux to easterly anomalies. This means that most El Niño events do not generate concurrent IOD events. Further, an unrealistic representation of the model's Java–Timor geometry resulted in an artificial pathway for El Niño upwelling Rossby waves to reach the model Java coast, resulting in a spurious oceanic teleconnection. In that model, several seasons after an El Niño peaks, the Pacific thermocline is at its shallowest depth, as a result of heat discharge (Jin 1997). The upwelling wave reaches the Java coast in the model, lifts the thermocline, and leads to a positive IOD in the following winter and spring. Analysis of observations, however, shows that there is no pathway for Pacific Rossby waves to reach the Java coast (Cai et al. 2005; Shi et al. 2007).

It turns out that this spurious oceanic teleconnection is also generated in several other models as well as CSIRO Mk3.0 [CNRM-CM3, CSIRO Mk3.5, BCCR CM2.0, and MIROC3.2(medres)], where the correlation between time series of the IOD and ENSO peaks at lag +1 yr; that is, the IOD tends to occur in the following year after an El Niño peaks (Table 1). For CNRM-CM3 and BCCR CM2.0 (as well as CSIRO Mk3.0), the correlation at lag 0 is not significant, suggesting a weak atmospheric teleconnection with ENSO. For MIROC3.2(medres) and CSIRO Mk3.5, the IOD can occur concurrently with El Niño as shown by a significant correlation at lag 0, which suggests that a somewhat more realistic atmospheric teleconnection

TABLE 1. Lag correlation between ENSO and the IOD using time series of indices in SON, and standard deviations of seasonal ENSO indices in four CMIP3 models.

	ENSO and IOD		ENSO seasonality			
	Lag 0	Lag+1 yr	DJF	MAM	JJA	SON
CNRM-CM3	0.10	0.74	1.81	1.39	1.02	1.43
CSIRO-Mk3.0	0.27	0.73	0.96	0.84	0.85	0.93
CSIRO-Mk3.5	0.60	0.65	1.08	1.20	1.11	1.09
BCCR-CM2.0	0.23	0.49	0.87	0.84	0.63	0.90
MIROC3.2(medres)	0.38	0.55	0.57	0.42	0.57	0.69

operates. However, because of the spurious oceanic teleconnection, IOD events tend to also occur in the proceeding years. Previous studies have shown that in these two models, both the equatorial Pacific waveguide and the subtropical North Pacific waveguide are involved in the ENSO discharge and recharge signals that are transmitted to the Indian Ocean (Cai et al. 2009c).

To illustrate the post–El Niño discharge in these five models and its relationship to the elevated Indian Ocean thermocline in the year after El Niño peaks, we applied EOF analysis to the model SON D20 anomalies in the tropical Pacific Ocean and Indian Ocean domain of 15°S–15°N. The first two EOFs are plotted in Fig. 11 and the associated time series in Fig. 12. The recharge–discharge paradigm of ENSO (Jin 1997) and observational supporting evidence (Meinen and McPhaden 2000) suggest that EOF1 and EOF2 of D20 reflect different phases of the ENSO cycle.

The first mode has an out-of-phase structure across the equatorial Pacific basin associated with the west–east transfer of warm water that accompanies mature ENSO conditions and is highly correlated with the Niño-3.4 index, with correlation coefficients ranging from 0.78 to 0.94 (the lowest correlation is in CSIRO Mk3.5, due to an unrealistic seasonality of ENSO, as will be discussed later). The second mode represents the zonal-mean shoaling of the equatorial Pacific thermocline (Fig. 11, right column), that is, the discharge of the zonal-mean equatorial Pacific heat content approximately a quarter period after an El Niño event peaks. The EOF patterns (Fig. 11) and the time series (Fig. 12) together show that an El Niño leads to a discharged equatorial Pacific. The strong negative weights off the Sumatra–Java coast (Figs. 11f and 11h) reflect the spurious effect of propagation of the upwelling Rossby wave from the Pacific into the equatorial Indian Ocean waveguide (oceanic teleconnection), common to all five models. Reversing the sign of EOF2 in both the pattern and the time series would mean that a recharged equatorial Pacific precedes an El Niño event.

Two models (CNRM-CM3 and CSIRO Mk3.0) display no ENSO-concurrent negative weights (shallowing of the thermocline) in the eastern Indian Ocean (Figs. 11a and 11b), which are present in the observed and triggered by ENSO-induced surface easterly anomalies over the eastern Indian Ocean through the atmospheric teleconnection. Instead, strong anomalies are generated in the spring season of the following year (showing a maximum correlation at 1-yr lag, Table 1), indicating a discharge signal reaching the Sumatra–Java coast and lifting the thermocline.

The behavior of the other 3 models [CSIRO Mk3.5, BCCR CM2.0, and MIROC3.2(medres)] is somewhat similar to each other, displaying a seemingly realistic response to El Niño with a concurrent uplift of the thermocline in the eastern Indian Ocean (Figs. 11c and 11e) by ENSO-induced easterly wind anomalies, and hence some concurrent IODs. In MIROC3.2(medres), ENSO tends to peak in SON (Table 1), favorable for concurrent IOD occurrence. In CSIRO Mk3.5, ENSO peaks in MAM (Table 1) rather than the observed DJF, and "concurrent" IOD events actually occur in the ensuing austral winter and spring seasons (one to two seasons later). In addition, because a similar spurious oceanic teleconnection operates, some IOD events are also generated in the winter and spring in the proceeding year. This is one reason why there is a large number of two consecutive positive IOD events in this model (Cai et al. 2009b).

To further illustrate the control of the oceanic teleconnection on the IOD in the CSIRO Mk3.5, Fig. 13 compares the evolution associated with the ENSO recharge–discharge mode (EOF2, a positive value indicates ENSO discharge as in Figs. 11g and 12c) and the thermocline anomalies associated with the model SON IOD index. A resemblance is seen in both a showing a transmission of Pacific signals to the Sumatra–Java coast continuing into austral spring in the following year and a preconditioning an uplift of the thermocline (D20) in the Sumatra–Java region favorable for positive IOD development. The evolutions for BCCR-CM2.0 and MIROC3.2(medres) are similar (figure not shown).

The large control by ENSO on the IOD in these five models contributes to a strong control by ENSO on the IOD in the multimodel space shown in Fig. 10b. As discussed earlier, without an adjustment for the maximum correlation at the 1-yr lag, the correlation of the linear fit is smaller.

In summary, CMIP3 models confirm a mutual influence between the IOD and ENSO, although most models produce an ENSO–IOD correlation that is too weak. However, the control of ENSO on the IOD is enhanced by a spurious oceanic teleconnection in five models.

6. Discussion and conclusions

The present study focuses on the relationship among the three major global climate drivers in the CMIP3

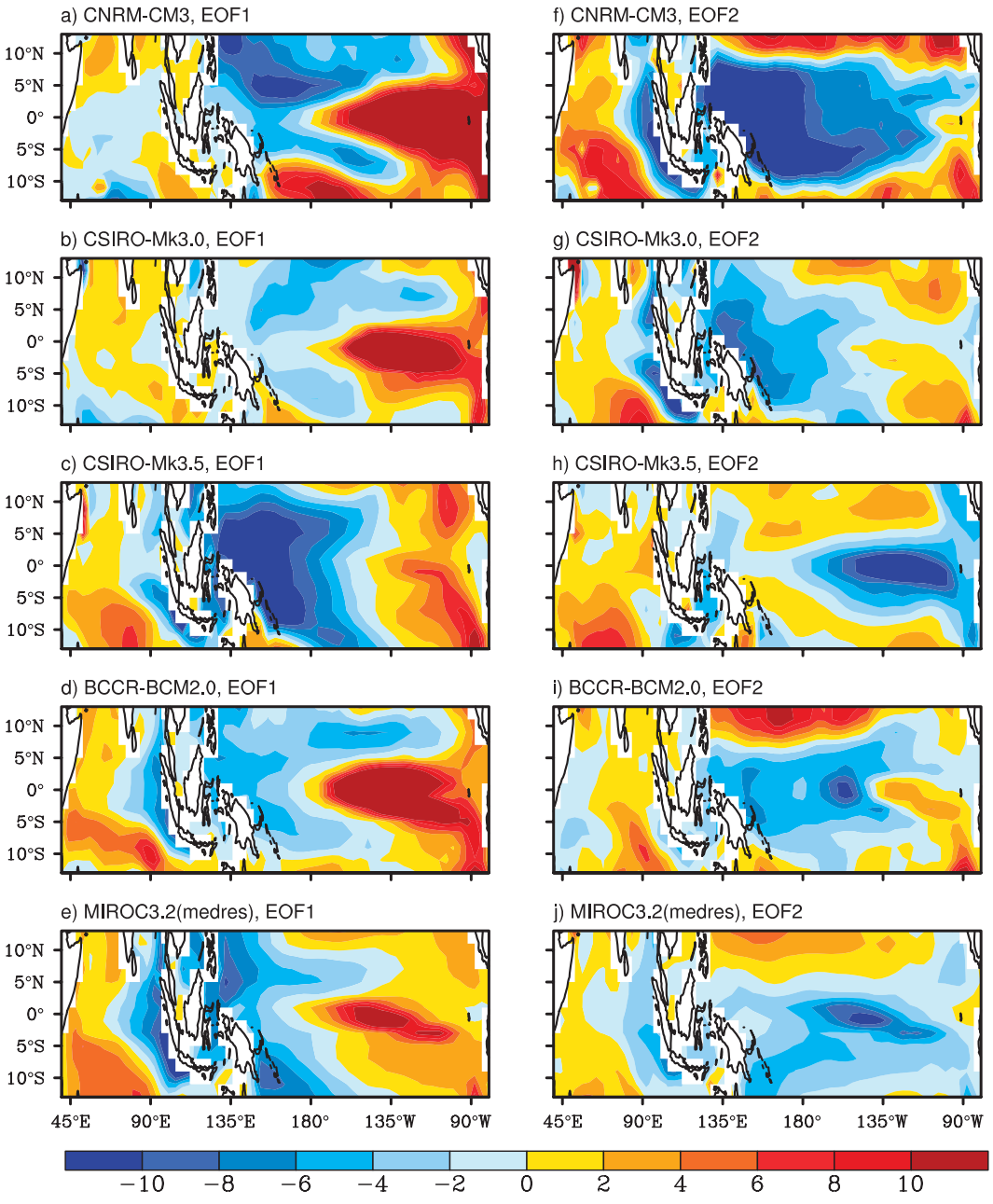

FIG. 11. (a)–(e) EOF1 and (f)–(j) EOF2 of SON D20 in the Indo-Pacific domain (15°N–15°S, 40°E–80°W) for the 5 models that simulate a spurious oceanic teleconnection, leading to the feature that positive IOD events occur in the year after El Niño peaks.

models. Each model, like the only realization in the real world, has its own variability, the properties of which could be rather different on multi-decade, or multi-century time scales, as revealed by multi-century-long experiments (Wittenberg 2009). Thus, even if these models are perfect, one expects vastly different properties from one model to another, given that we only take 50-yr samples from each model. However, as the multimodel space represents a spectrum of possible climate regimes, an aggregation of properties in these models allows an examination of issues beyond the performance of individual models, including the likelihood of a SAM driving positive IOD events or the IOD's influence on ENSO events. When addressed using an individual model, any outcome is subject to the possibility of being a particular character of that model or chosen period.

Several important conclusions emerge. First, the models ENSO signals project strongly onto the SAM, and

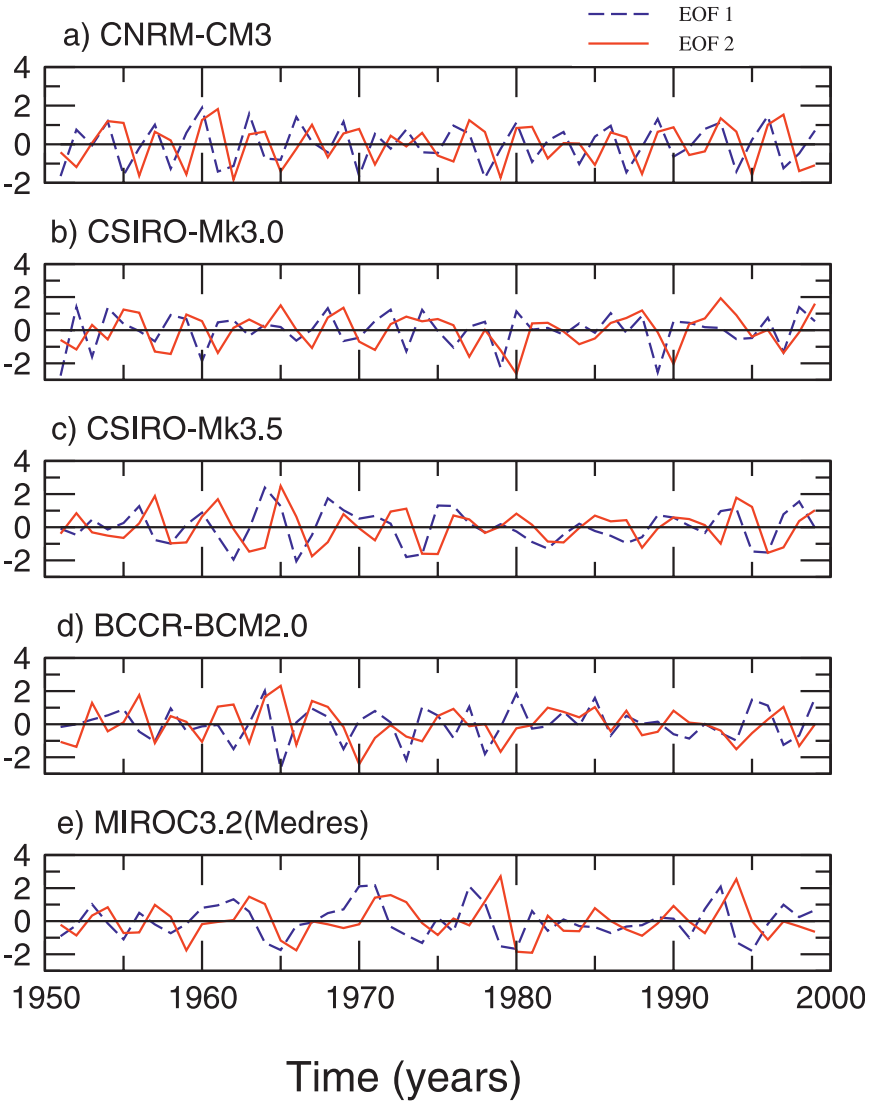

FIG. 12. Time series associated with EOF1 (concurrent with ENSO, blue dash) and EOF2 (the ENSO discharge mode, red solid) of the five models shown in Fig. 11.

similarly to other modes (e.g., the PSA); the ENSO-forced signal tends to peak before ENSO. In a way, this is similar to the situation associated with the IOD. The IOD-induced signal over south of Australia, through stationary equivalent barotropic wave trains, peaks before the IOD itself. Second, there is little control by the SAM on the IOD, in contrast to what was suggested previously. Indeed, no model produces a SAM–IOD relationship that supports a positive SAM driving a positive IOD event. This is the case even in models in which there is virtually no relationship between ENSO and the IOD. Third, although most models simulate a relationship between ENSO and the IOD that is far weaker than the observed, ENSO does exert an influence over the IOD. However, this influence is boosted by a spurious oceanic teleconnection, whereby the ENSO discharge–recharge signal transmits to the Sumatra–Java coast, instead of the NWA coast as observed, changing the thermocline in the eastern Indian Ocean and the IOD properties. Without this spurious oceanic teleconnection, the influence of the IOD on ENSO is comparable to the impact of ENSO on the IOD.

We have highlighted a number of common model deficiencies as shown in numerous studies (e.g., AchutaRao and Sperber 2002; Guilyardi 2006; Joseph and Nigam 2006; Cai et al. 2009c), in addition to the spurious Indo-Pacific oceanic teleconnection. These include an overly strong model IOD, too strong model SAM, as well as

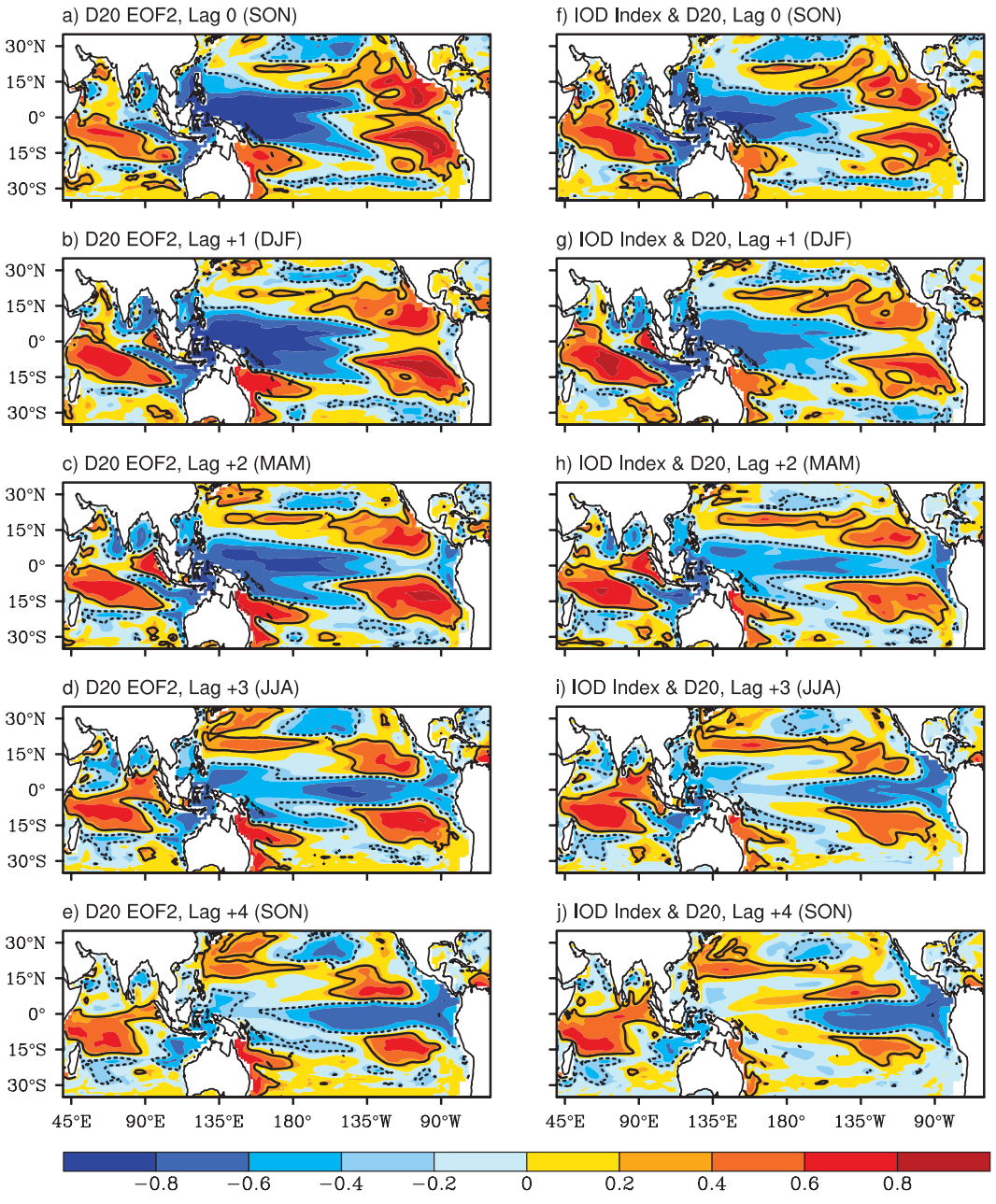

FIG. 13. (a)–(e) Evolution (displayed as seasonal lag correlations) of gridpoint D20 anomalies associated with the time series of D20 EOF2 (red curve of Fig. 12c, CSIRO-Mk3.5 in SON), i.e., the ENSO discharge–recharge mode. (f)–(j) As in (a)–(e), but with CSIRO-Mk3.5 IOD in SON. Lags refer to seasonal lags moving forward 3 months at a time. Areas confined by contours indicate statistical significance at the 95% confidence level.

an unrealistic ENSO seasonal phase locking in some models. Alleviations of these model defects may improve simulation of the relationships among these climate drivers.

Acknowledgments. This work is supported by the Australian Climate Change Science Program. We recognize the many models used as part of the Program for Climate Model Diagnosis and Intercomparison (PCMDI) to produce the CMIP3 database.

REFERENCES

AchutaRao, K., and K. Sperber, 2002: Simulation of the El Niño Southern Oscillation: Results from the Coupled Model Intercomparison Project. *Climate Dyn.,* **19,** 191–209.

Alexander, M. A., I. Bladé, M. Newman, J. R. Lanzante, N.-C. Lau, and J. D. Scott, 2002: The atmospheric bridge: The influence of ENSO teleconnections on air–sea interaction over the global oceans. *J. Climate,* **15,** 2205–2231.

Annamalai, H., S. P. Xie, J. P. McCreary, and R. Murtugudde, 2005: Impact of Indian Ocean sea surface temperature on developing El Niño. *J. Climate,* **18,** 302–319.

Behera, S. K., J. J. Luo, S. Masson, S. A. Rao, H. Sakuma, and T. Yamagata, 2006: A CGCM study on the interaction between IOD and ENSO. *J. Climate,* **19,** 1688–1705.

Cai, W., and P. G. Baines, 2001: Forcing of the Antarctic circumpolar wave by El Niño-Southern Oscillation teleconnections. *J. Geophys. Res.,* **106,** 9019–9038.

——, and T. Cowan, 2007: Trends in Southern Hemisphere circulation in IPCC AR4 models over 1950–99: Ozone depletion versus greenhouse forcing. *J. Climate,* **20,** 681–693.

——, H. H. Hendon, and G. Meyers, 2005: Indian Ocean dipolelike variability in the CSIRO Mark 3 coupled climate model. *J. Climate,* **18,** 1449–1468.

——, A. Sullivan, and T. Cowan, 2009a: Climate change contributes to more frequent consecutive positive Indian Ocean dipole events. *Geophys. Res. Lett.,* **36,** L23704, doi:10.1029/2009GL040163.

——, ——, and ——, 2009b: How rare are the 2006–2008 positive Indian Ocean dipole events? An IPCC AR4 climate model perspective. *Geophys. Res. Lett.,* **36,** L08702, doi:10.1029/2009GL037982.

——, ——, and ——, 2009c: Rainfall teleconnections with Indo-Pacific variability in the WCRP CMIP3 models. *J. Climate,* **22,** 5046–5071.

Clarke, A. J., and X. Liu, 1994: Interannual sea level in the northern and eastern Indian Ocean. *J. Phys. Oceanogr.,* **24,** 1224–1235.

Godfrey, J., 1975: On ocean spindown I: A linear experiment. *J. Phys. Oceanogr.,* **5,** 399–409.

Guilyardi, E., 2006: El Niño-mean state-seasonal cycle interactions in a multi-model ensemble. *Climate Dyn.,* **26,** 329–348.

——, A. Wittenberg, A. Fedorov, M. Collins, C. Wang, A. Capotondi, G. J. van Oldenborgh, and T. Stockdale, 2009: Understanding El Niño in ocean–atmosphere general circulation models: Progress and challenges. *Bull. Amer. Meteor. Soc.,* **90,** 325–340.

Hendon, H., 2003: Indonesian rainfall variability: Impacts of ENSO and local air–sea interaction. *J. Climate,* **16,** 1775–1790.

Hobbs, W. R., and M. N. Raphael, 2007: A representative time-series for the Southern Hemisphere zonal wave 1. *Geophys. Res. Lett.,* **34,** L05702, doi:10.1029/2006GL028740.

Hoskins, B. J., and D. J. Karoly, 1981: The steady linear response of a spherical atmosphere to thermal and orographic forcing. *J. Atmos. Sci.,* **38,** 1179–1196.

Hughes, C. W., P. L. Woodworth, M. P. Meredith, V. Stepanov, T. Whitworth, and A. R. Pyne, 2003: Coherence of Antarctic sea levels, Southern Hemisphere annular mode, and flow through Drake Passage. *Geophys. Res. Lett.,* **30,** 1464, doi:10.1029/2003GL017240.

Ivchenko, V. O., V. B. Zalesny, and M. R. Drinkwater, 2004: Can equatorial ocean quickly respond to Antarctic sea ice/salinity anomalies? *Geophys. Res. Lett.,* **31,** L15310, doi:10.1029/2004GL020472.

——, ——, ——, and J. Schröter, 2006: A quick response of the equatorial ocean to Antarctic sea ice/salinity anomalies. *J. Geophys. Res.,* **111,** C10018, doi:10.1029/2005JC003061.

Izumo, T., and Coauthors, 2010: Influence of the state of the Indian Ocean dipole on the following year's El Niño. *Nat. Geosci.,* **3,** 168–172, doi:10.1038/ngeo760.

Jin, D., and B. P. Kirtman, 2009: Why the Southern Hemisphere ENSO responses lead ENSO. *J. Geophys. Res.,* **114,** D23101, doi:10.1029/2009JD012657.

Jin, F.-F., 1997: An equatorial ocean recharge paradigm for ENSO. Part I: Conceptual model. *J. Atmos. Sci.,* **54,** 811–829.

Joseph, R., and S. Nigam, 2006: ENSO evolution and teleconnections in IPCC's twentieth-century climate simulations: Realistic representation? *J. Climate,* **19,** 4360–4377.

Kalnay, E., and Coauthors, 1996: The NCEP/NCAR 40-Year Reanalysis Project. *Bull. Amer. Meteor. Soc.,* **77,** 437–471.

Karoly, D. J., 1989: Southern Hemisphere circulation features associated with El Niño–Southern Oscillation events. *J. Climate,* **2,** 1239–1252.

Kidson, J. W., and J. A. Renwick, 2002: The Southern Hemisphere evolution of ENSO during 1981–99. *J. Climate,* **15,** 847–863.

Klein, S. A., B. J. Soden, and N.-C. Lau, 1999: Remote sea surface temperature variations during ENSO: Evidence for a tropical atmospheric bridge. *J. Climate,* **12,** 917–932.

Kug, J.-S., and I.-S. Kang, 2006: Interactive feedback between ENSO and the Indian Ocean. *J. Climate,* **19,** 1784–1801.

Lau, N.-C., and M. J. Nath, 2004: Coupled GCM simulation of atmosphere–ocean variability associated with zonally asymmetric SST changes in the tropical Indian Ocean. *J. Climate,* **17,** 245–265.

L'Heureux, M. L., and D. W. Thompson, 2006: Observed relationships between the El Niño–Southern Oscillation and the extratropical zonal-mean circulation. *J. Climate,* **19,** 276–287.

Li, T., B. Wang, C.-P. Chang, and Y. Zhang, 2003: A theory for the Indian Ocean dipole–zonal mode. *J. Atmos. Sci.,* **60,** 2119–2135.

Luo, J.-J., S. Masson, S. K. Behera, and T. Yamagata, 2008: Extended ENSO predictions using a fully coupled ocean–atmosphere model. *J. Climate,* **21,** 84–93.

——, R. Zhang, S. K. Behera, Y. Masumoto, F.-F. Jin, R. Lukas, and T. Yamagata, 2010: Interaction between El Niño and extreme Indian Ocean dipole. *J. Climate,* **23,** 726–742.

Marshall, G., 2003: Trends in the southern annular mode from observations and reanalyses. *J. Climate,* **16,** 4134–4143.

Meinen, C. S., and M. J. McPhaden, 2000: Observations of warm water volume changes in the equatorial Pacific and their relationship to El Niño and La Niña. *J. Climate,* **13,** 3551–3559.

Meredith, M. P., P. L. Woodworth, C. W. Hughes, and V. Stepanov, 2004: Changes in the ocean transport through Drake Passage during the 1980s and 1990s, forced by changes in the southern annular mode. *Geophys. Res. Lett.,* **31,** L21305, doi:10.1029/2004GL021169.

Philander, S. G., 1990: *El Niño, La Niña, and the Southern Oscillation*. Academic Press, 289 pp.

Potemra, J. T., 2001: Contribution of equatorial Pacific winds to southern tropical Indian Ocean Rossby waves. *J. Geophys. Res.,* **106,** 2407–2422.

Raphael, M. N., and M. M. Holland, 2006: Twentieth century simulation of the Southern Hemisphere climate in coupled models. Part 1: Large scale circulation variability. *Climate Dyn.,* **26,** 217–228.

Rayner, N. A., D. E. Parker, E. B. Horton, C. K. Folland, L. V. Alexander, D. P. Rowell, E. C. Kent, and A. Kaplan, 2003: Global analyses of sea surface temperature, sea ice, and night marine air temperature since the late nineteenth century. *J. Geophys. Res.,* **108,** 4407, doi:10.1029/2002JD002670.

Saji, N. H., and T. Yamagata, 2003a: Possible impacts of Indian Ocean dipole mode events on global climate. *Climate Res.,* **25,** 151–169.

——, and ——, 2003b: Structure of SST and surface wind variability during Indian Ocean dipole mode years: COADS observations. *J. Climate,* **16,** 2735–2751.

——, B. N. Goswami, P. N. Vinayachandran, and T. Yamagata, 1999: A dipole mode in the tropical Indian Ocean. *Nature,* **401,** 360–363.

——, S. P. Xie, and T. Yamagata, 2006: Tropical Indian Ocean variability in the IPCC twentieth-century climate simulations. *J. Climate,* **19,** 4397–4417.

Shi, G., J. Ribbe, W. Cai, and T. Cowan, 2007: Multidecadal variability in the transmission of ENSO signals to the Indian Ocean. *Geophys. Res. Lett.,* **34,** L09706, doi:10.1029/2007GL029528.

——, W. Cai, T. Cowan, J. Ribbe, L. Rotstayn, and M. Dix, 2008: Variability and trend of North West Australia rainfall: Observations and coupled climate modeling. *J. Climate,* **21,** 2938–2959.

Vivier, F., K. A. Kelly, and M. Harismendy, 2005: Causes of large-scale sea level variations in the Southern Ocean: Analyses of sea level and a barotropic model. *J. Geophys. Res.,* **110,** C09014, doi:10.1029/2004JC002773.

Wallace, J. M., and D. W. J. Thompson, 2002: The Pacific center of action of the Northern Hemisphere annular mode: Real or artifact? *J. Climate,* **15,** 1987–1991.

Webster, P. J., A. M. Moore, J. P. Loschnigg, and R. R. Leben, 1999: Coupled ocean-atmosphere dynamics in the Indian Ocean during 1997–98. *Nature,* **401,** 356–360.

Wijffels, S., and G. A. Meyers, 2004: An intersection of oceanic wave guides: Variability in the Indonesian Throughflow region. *J. Phys. Oceanogr.,* **34,** 1232–1253.

Wittenberg, A. T., 2009: Are historical records sufficient to constrain ENSO simulations? *Geophys. Res. Lett.,* **36,** L12702, doi:10.1029/2009GL038710.

Xie, S.-P., H. Annamalai, F. A. Schott, and J. P. McCreary Jr., 2002: Structure and mechanisms of south Indian Ocean climate variability. *J. Climate,* **15,** 864–878.

——, K. Hu, J. Hafner, H. Tokinaga, Y. Du, G. Huang, and T. Sampe, 2009: Indian Ocean capacitor effect on Indo–Western Pacific climate during the summer following El Niño. *J. Climate,* **22,** 730–747.

Yulaeva, E., and J. M. Wallace, 1994: The signature of ENSO in global temperature and precipitation fields derived from the Microwave Sounding Unit. *J. Climate,* **7,** 1719–1736.